Proceedings of the 31st
Risø International Symposium on Materials Science:
Challenges in materials science and possibilities in 3D and 4D characterization techniques
Editors: N. Hansen, D. Juul Jensen,
S.F. Nielsen, H.F. Poulsen and B. Ralph
Risø National Laboratory for Sustainable Energy,
Technical University of Denmark, 2010

MICROSTRUCTURAL CHARACTERIZATION AND EVOLUTION IN 3D

S. R. Wilson[1], C. Hefferan[2], S. F. Li[2], R. M. Suter[2] and A. D. Rollett[1]

[1]Dept. Materials Science & Engineering
[2]Department of Physics
Carnegie Mellon University
Pittsburgh, PA 15213, USA

ABSTRACT

Advances in three-dimensional materials science are reviewed and examples of progress in characterization and evolution are given. One example concerns the measurement of mean width or integrated mean curvature. This quantity is attractive both because it is an additive, linear measure of size and because it is central to the theory of grain growth in three dimensions. A large Potts model of grain growth is used to provide data sets, from which the distributions of mean width form two bell curves, one for shrinking grains, and one for growing grains. A second example is given of analysis of grain boundary motion characterized by a non-destructive high-energy x-ray diffraction method. A minority of grains exhibit motion whereas the majority remain stationary. The 5-parameter grain boundary character distribution is compared for the mobile versus stationary boundaries.

1. INTRODUCTION

Microstructural evolution covers a wide range of phenomena. In this instance we review recent developments at the mesoscopic scale that are relevant to grain growth and recrystallization, with a particular emphasis on dealing with three-dimensional microstructures. The paper provides some information on a new aspect of materials characterization in 3D, along with an example of how to apply a detailed analysis of grain boundary motion in terms of all five degrees of freedom, i.e. misorientation and interface normal.

The characterization of shapes in three-dimensional images has become important in many branches of science and engineering, including biomedicine, geophysics, astrophysics, robotics, and materials science (to name only a few). Negligible communication between these disparate research communities and the mathematicians who have made significant advances in this

domain over the past century has led to several re-discoveries of Minkowski functionals as the appropriate measures of geometric size. These re-discoveries have, in turn, spawned redundant efforts to estimate the Minkowski functionals over pixellated data sets. Average grain size, for example, can be critical in determining macroscopic properties of materials. Many linear measures of size exist for three-dimensional objects, and an elaborate convention has been created to standardize this measure across the field. In the past, which linear measure to choose was not important to materials scientists due to the paucity of data. Recently, however, the advent of automated serial sectioning and synchrotron-based tomography and diffraction experiments, as well as statistical reconstructions of various kinds, have provided substantial amounts of data. In addition, there have been significant developments in methods for modeling microstructural evolution in 3D, including Monte Carlo, cellular automata, phase field and moving finite elements, to name only the most popular. Choosing the most appropriate linear measure of grain size with which to analyze and interpret the results of both experimental and computational efforts has therefore assumed greater importance.

At the most fundamental level, computational models require an exact theory against which they can be verified. For curvature-driven grain growth in 3D, MacPherson and Srolovitz have provided such a theory, and simulations show good agreement with the theory, Uyar *et al.* (2009). Central to the theory is the quantity mean width or integrated mean curvature, which is the only additive linear measure of size and which has interesting characteristics such as nearly Gaussian distributions. Such theories are limited, however, to uniform (isotropic) boundary conditions whereas real grain boundaries are strongly anisotropic. Recent measurements of grain boundary networks have permitted comparisons that take account of all five macroscopic degrees of freedom. For grain boundary energy in nickel, for example, the experimental and theoretical (from atomistic simulation) values show good agreement. However, the (inverse) correlation between grain boundary population and theoretical energy turns out to be more robust.

2. MEASUREMENTS ON IMAGES

There are a great variety of measurements that can be made on images of polycrystalline structures. The obvious measurement is that of volumes of grains since those can be obtained by simply counting the number of voxels associated with a given orientation. In measured microstructures, however, there are many steps that have to be taken before it is appropriate to carry out this, or any other measurement. There are always orientation gradients within grains, even in a well-annealed material, and some decisions are required to segment an image into distinct regions. These issues have, however, been already been adequately addressed (Uchic *et al.* 2006; Rollett *et al.* 2009). Another measurement that can readily be made directly on the image is that of boundary areas, which can be accomplished by counting voxels that are adjacent to boundaries. Partitioning voxels into bulk versus boundary-adjacent only requires inspection of nearest neighbor voxels. Measuring the linear size of 3D objects is, however, less obvious in terms of choosing a measure. Two traditional measures are to use the sphere-equivalent radius (or diameter) obtained from the volume measurement, or to use a linear intercept method. The former suffers from the obvious defect that it is not an independent measurement and involves an assumption about shape. Linear intercepts require further decisions when used on non-convex objects. Instead, a better choice may be that of integrated mean curvature, also known as mean width or mean breadth. The reasons to use this are that it is independent of volume or area, it shares the property of additivity (MacPherson and Srolovitz, 2008) and it is directly relevant to grain growth in 3D because it is one of the quantities needed to calculate the driving force for growth or shrinkage of grains. A crucial theorem due to Hadwiger (Klain and Rota,

1997, theorem 8.3.2) states that, up to an arbitrary multiplicative constant, for every dimension n, there exists one and only one continuous measure $M(D)$ of an object D, of dimension n that satisfies the additivity rule: $M(D1 \cup D2) = M(D_1)+M(D_2)-M(D_1 \cap D_2)$. In 3D, volume and area satisfy this rule almost intuitively, but it is not immediately obvious that there should be a linear measure that can do this. However, the linear Minkowski functional known as mean width does so and, we believe, should therefore be adopted in the materials science community as the fundamental linear measure of size for 3D objects. Mean width is most easily understood in the special case of convex bodies, for which it is equal to twice the mean caliper diameter.

Mean width algorithm. For computationally feasible grid dimensions, the exact mean width of a voxellized object represented on a grid does not approximate the mean width of the original object very well. The reason for this may be understood by considering the class of smooth objects. The mean width of a smooth object is proportional to the mean curvature integrated over its surface, and clearly the additional edges and corners introduced by the voxellated data artificially augment the estimate. To circumvent this difficulty, we focus on an algorithm developed by Ohser and Mücklich (2000), which we briefly describe and generalize below.

Assuming the object whose mean width is to be determined satisfies certain regularity conditions (realized in most realistic grain structures), Ohser and Mücklich use an integral expression for the mean width (Crofton's formula) to derive an expression that specifies how the local neighborhood of any given voxel determines its contribution to the mean width. To use this expression for a given binary image, it is possible, as Ohser and Mücklich suggest, to construct a "histogram" that records a frequency count of neighborhoods over all voxels. The mean width is then computed by multiplying the contribution from every neighborhood type by the number of such neighborhoods in the grid and then summing over the entire histogram.

We were not satisfied with initial tests of Ohser and Mücklich's algorithm, and so we looked for ways to improve upon it. Their algorithm includes a discretization of an integral over the unit sphere. For reasons related to memory storage, Ohser and Mücklich integrate over a special set of directions (all low-index directions, up to and including <111>). In order to incorporate more directions, we chose to eliminate construction of the histogram. In this way, neighborhood information need not be stored, and so we can sample many more lattice directions. Moreover, intermediate histogram construction limits the application of the algorithm to binary image data, so that performance is linear in the number of grains. Neglecting this step also permits us to focus only on the non-zero grains in the neighborhood of any single datapoint. We are thus able to process thousands of grains in almost the same time it takes Ohser and Mücklich's program to process a single grain.

We wished to determine and compare the numerical errors inherent in both the original formulation of Ohser and Mücklich's method and our slight generalization. To do so, we considered five families of test shapes, whose mean widths can be exactly computed: (1) regular polyhedra; (2) spheroids; (3) lemons (the arc of a circle, rotated about its chord); and (4) lenses (spherical cap, joined with its reflection). Figure 1 shows the geometry and notation associated with lens shapes. Figure 2 shows images of the lens and lemon shapes. These shapes allow us to separate errors due to curved

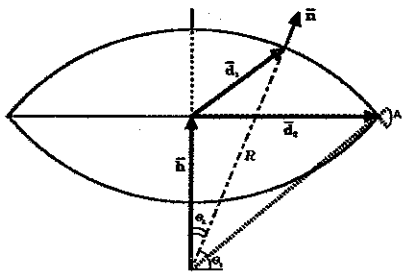

Fig. 1. Geometry of lens-shaped objects.

surfaces, nodes, and facets.

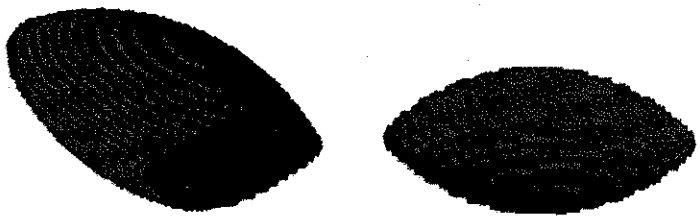

Lens	Lemon
radius of curvature R	radius of curvature R
dihedral angle A	cone angle A at each cusp
$4R\left[\frac{A}{4}\cos\frac{A}{2}-\sin\frac{A}{2}+1\right]$	$4R\cos\frac{A}{2}-R(\pi-A)\sin\frac{A}{2}$

Fig. 2. Illustrations of a lens-shaped object and a lemon shaped object, with their geometries.

Analytical expressions for mean widths of both lenses and lemons are obtained by directly averaging the caliper diameter over all possible directions and multiplying by two. This requires integration over all directions $\dot{n}$=(sinθ cosφ, sinθ sinφ, cosθ), where θ is the angle between $\dot{n}$ and the z-axis. Because the lemon and the lens are both convex, every direction $\dot{n}$ is associated with a single surface point. The z-axis is aligned with the symmetry axis in both cases – cusp to cusp, for the lemon; and through the smallest diameter, for the lens. Denote by $\dot{d}$ the vector from the center to any surface point of either shape. The mean caliper diameter associated with this direction is then $2\,\dot{d}\cdot\dot{n}$. Using the notation from the figure, the integrals we need to compute both have the form:

$$M=\frac{1}{\pi}\int_{\alpha_1}^{\alpha_2}d\theta\sin\theta\int_0^{2\pi}d\phi 2\vec{d}_1\cdot\vec{n}+\frac{1}{\pi}\int_{\beta_1}^{\beta_2}d\theta\sin\theta\int_0^{2\pi}d\phi 2\vec{d}_2\cdot\vec{n} \tag{1}$$

For the lemon it can be seen that α_1 = A/2, α_2 =(π−A)/2, β_1 =0, and β_2 =A/2. From the figure we also have:

$$\vec{d}_1\cdot\vec{n}=R-\vec{h}\cdot\vec{n}=R-R\sin(A/2)\sin\theta$$
and
$$\vec{d}_2\cdot\vec{n}=R\sin(A/2)\cos\theta \tag{2}$$

Similarly for the lens, α_1 = 0, α_2 = (π − A)/2, β_1 = (π−A)/2, and β_2 = π/2. Again from the figure:

$$\vec{d}_1 \cdot \vec{n} = R - R\sin(A/2)\cos\theta$$
and
$$\vec{d}_2 \cdot \vec{n} = R\sin(A/2)\sin\theta$$

(3)

Evaluating the integrals in Eq. 1 for each shape leads to the analytical forms listed in Table 1. To compare analytical expressions with estimations on regular grids, we created characteristic functions centered on a single grid point. In order to investigate directional error, we rotated the z-axis and sampled the characteristic function at the transformed grid points. Average mean widths and standard deviations over many rotations for the shapes selected for this study are listed in Table 1. Note that two different algorithms were used to generate this table. Columns (3) and (4) represent output from the algorithm (O&M) given directly by Ohser and Mücklich, whereas columns (5) and (6) were generated by a generalized algorithm (MW211) that includes all low-index planes up to and including the (211) family of planes. All distances, volumes, and mean widths are given in voxels; for the regular polyhedra, S represents the edge length.

The agreement between theory and computation at the resolutions listed in this table are exceptional for both algorithms and across all orientations. The low standard deviations indicate that there is virtually no directional anisotropy in the algorithm induced by the underlying grid. Though both algorithms perform very well, we note in passing that the standard deviations obtained from MW211 are significantly lower than O&M in most cases, and (except for the lemon) values obtained from MW211 are more accurate than from O&M.

Table 1. Relative mean width errors for various resolutions.

	Parameters	Theory	O&M	Percent error	MW211	Percent error
spheroid	a = 60; b = 10	128.38	128.21±1.13	-0.12	128.26±0.77	-0.09
lens	R = 23; A = 62°	66.91	67.16±0.50	0.38	66.98±0.27	0.11
lemon	R = 23; A = 62°	69.09	69.13±0.33	0.05	68.97±0.21	-0.17
tetrahedron	S = 20	36.49	37.02±1.28	-1.44	36.61±0.99	0.32
cube	S = 20	60.00	59.18±2.58	-1.36	59.76±1.58	-0.41
octahedron	S = 20	94.04	93.80±2.10	-0.25	94.11±1.01	0.07
isocahedron	S = 20	69.68	69.26±0.68	-0.60	69.15±0.37	-0.77
dodecahedron	S = 20	105.73	106.40±0.95	0.64	106.56±0.73	-0.15

Because our simulated microstructures often contain grains much smaller than the resolution used to determine Table 1, a study of error with resolution is summarized in Fig. 3 for the polyhedral objects and in Fig. 4 for objects with curved surfaces. Note that in this study, error could be categorized by morphology: faceted shapes lead to much larger error than shapes with curved surfaces. We find that a good estimate of the percent error involved for a faceted shape of mean width M voxels is simply equal to M/100.

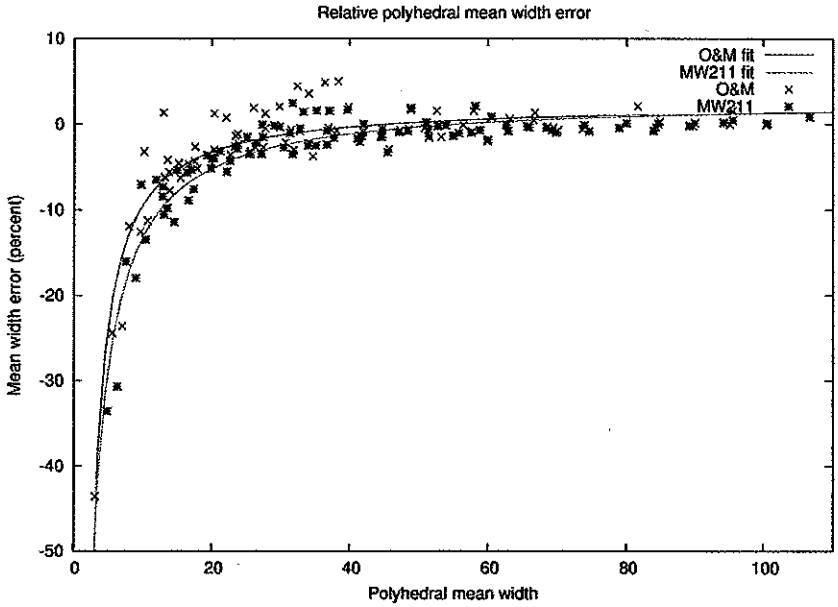

Fig. 3. Error in the measurement of mean width for various polyhedra as a function of size.

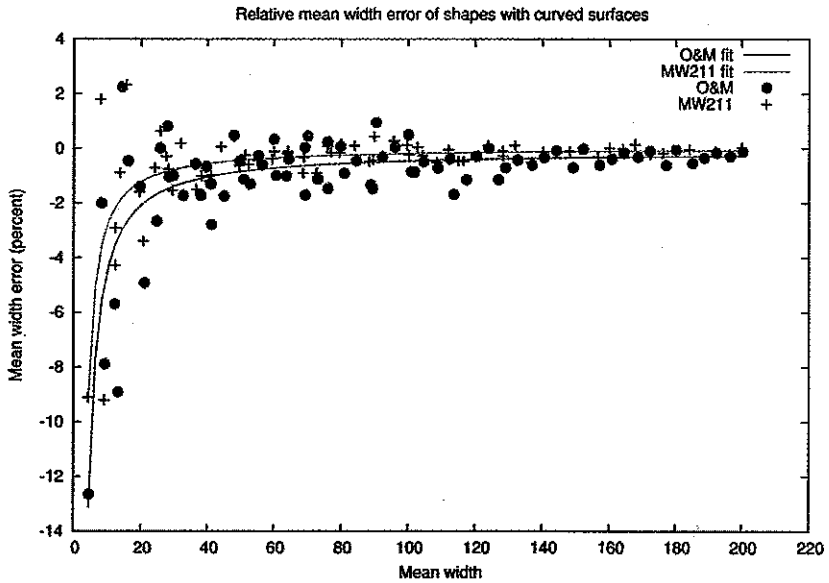

Fig. 4. Error in the measurement of mean width for shapes with curved surfaces as a function of size. Note the smaller values on the vertical scale for error as compared with the previous figure.

Figure 5 summarizes a study of the error dependence for the special case of the lens. We studied the lens in more detail. We fix the base radius of the lens and vary the dihedral angle subtended

along the crease, allowing both convex and concave geometries (given by positive and negative dihedral angles, respectively). Two such lenses are depicted in this figure (with base radii 50 and 60 voxels, respectively). Zero dihedral angle corresponds to the sphere, whereas the largest dihedral angle approaches a thin disk. Excellent agreement is obtained for all dihedral angles.

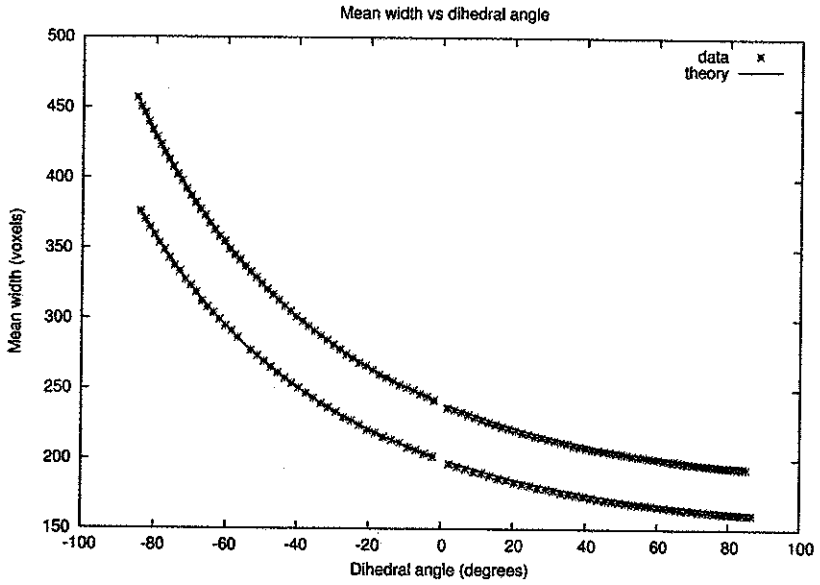

Fig. 5. Comparison of the measured (points) versus the theoretical (continuous line) mean width values for lens-shaped objects with two different values of their base radii, namely radii 50 (lower curve) and 60 voxels (upper curve).

Mean width distribution in Polycrystal: In order to illustrate the capability of the mean width measurement algorithm, a standard isotropic Potts model was used to simulate grain growth on a grid of dimensions 1000 cubed using the parallel MMSP grid library (MMSP, 2010) developed and maintained by Gruber. The large domain size was used to minimize mean width resolution error, as well as to permit adequate statistics following significant coarsening. Due to the size of the grid, initial grain ids were assigned using a simple checkerboard tessellation consisting of cubes of edgelength 5 voxels, so that the initial microstructure was composed of nearly 8 million unique grains. During evolution, the mean width and the volume of all surviving grains were computed after back-to-back MC steps every 100 MC timesteps (e.g., after the 99th and 100th timesteps).

The initial checkerboard tessellation required a significant relaxation period before the system attained a steady-state mean width distribution. In Fig. 6, the average mean width is plotted as a function of time. It is seen that the expected square root evolution only begins after approximately 1700 timesteps. However, a better measure of whether steady state has been achieved is perhaps obtained by plotting the ratio of the number N_g of growing grains to the number N_s of shrinking grains, where growth rate is determined by any observed volume change between subsequent time steps. The ratio N_s/N_g is plotted in Fig. 7, from which it can be seen that steady state is not attained until after roughly 3000 timesteps, at which point there are approximately 5 shrinking grains for every 3 growing grains in the system.

The measured mean width distribution after 3600 MC steps is shown in Fig. 8, at which point

17,338 grains of average mean width 48.304 voxels remained in the domain. We note that this distribution is clearly not lognormal.

The MacPherson-Srolovitz relation relates the rate at which the volume of an individual grain changes directly to its mean width, and so it is of interest to consider the mean width distributions for the subsets of growing and shrinking grains separately. These two histograms are depicted in Fig. 9. The remarkable observation is that if negative mean widths are discounted both may be fit to an excellent approximation by normal distributions. Each population is fit to the function $f(x)=A_i \exp(-(x-m_i)^2/2s_i^2)$, where m_i and s_i are measured directly from the data and listed in table 2, and A_i is the only adjustable parameter. At t=3600, the population of growing grains are fit by $A_1 = 161.705 \pm 1.56$ and shrinking grains by $A_2 = 262.794 \pm 2.516$. Note that, as a fraction of the total population mean, the means may be approximated by $4/\pi$ (for the growing distribution) and 4/5 (for the shrinking distribution). Also, the standard deviations for both distributions are both approximately equal to 1/3; the authors note that for this value the first inflection of the growing Gaussian occurs at the mean of the population as a whole. Lastly, we remark that $A_2/A_1 = 1.625$, in excellent agreement with N_s/N_g.

Table 2. Measured values of the mean and standard deviation at t=3600.

	Average mean width	Standard deviation
Total population	<M> = 48.304	0.4014<M>
Shrinking grain population	m_2=0.8246<M>	s_2=0.3324<M>
Growing grain population	m_1=1.2853<M>	s_1= 0.3347<M>

Although the authors do not currently have any explanation for these observations, it is noted that the measured histograms reflect the probability that a grain with a given mean width is either shrinking or growing. The MacPherson-Srolovitz relation shows that this is equivalent to the probability that the mean width of a grain is greater than (resp. less than) one-sixth of the summed length of all its triple junctions. This may suggest a theoretical approach to determining an analytical expression for the mean width distribution.

lomain. We note that this

me of an individual grain
consider the mean width
ly. These two histograms
egative mean widths are
nal distributions. Each

: m_i and s_i are measured
ole parameter. At t=3600,
and shrinking grains by
mean, the means may be
ıe shrinking distribution).
imately equal to 1/3; the
sian occurs at the mean of
excellent agreement with

ion at t=3600.

Standard deviation
0.4014<M>
s_2=0.3324<M>
s_1= 0.3347<M>

e observations, it is noted
th a given mean width is
/s that this is equivalent to
less than) one-sixth of the
al approach to determining

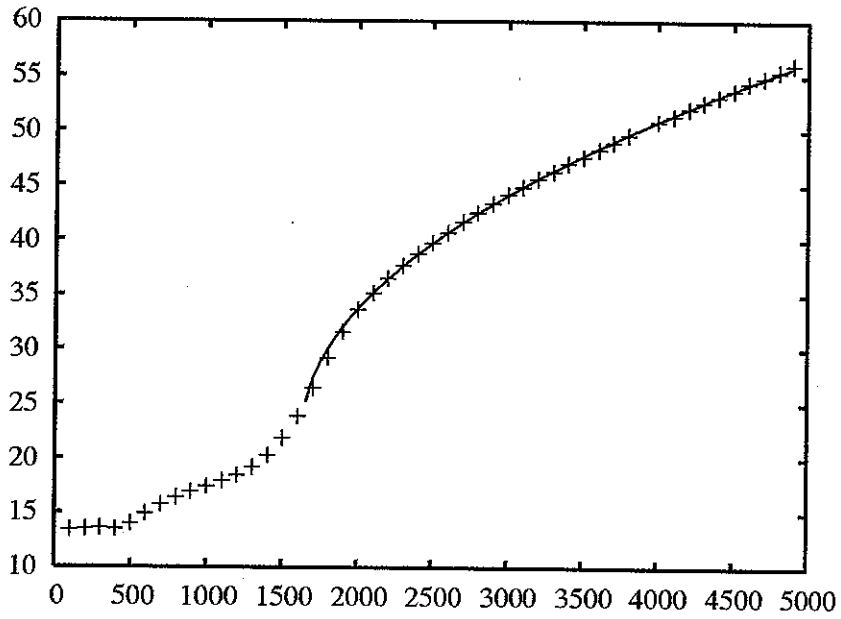

Fig. 6. A plot of the average mean width as a function of time in an isotropic Potts grain growth model (+). A fit to the expected square root dependence (solid line) is also plotted.

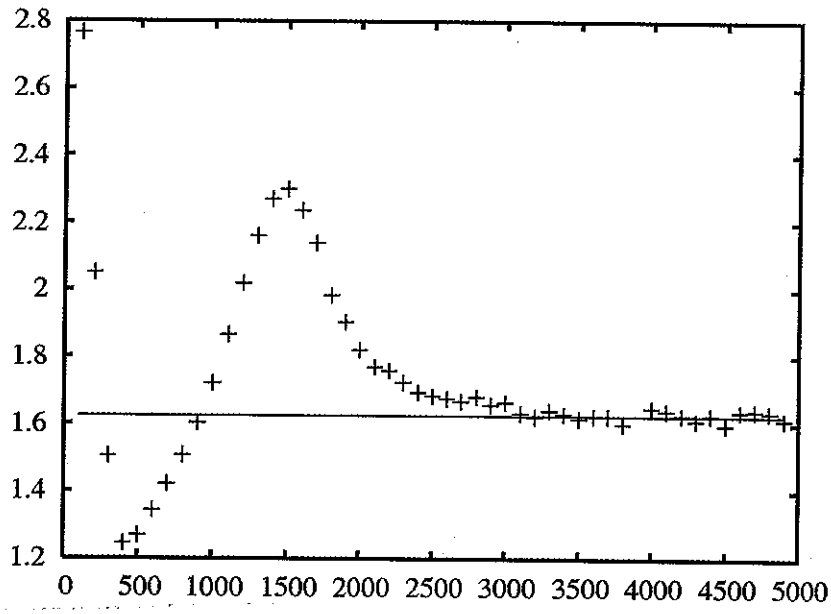

Fig. 7. The measured ratio of the number of shrinking grains to growing grains is plotted as a function of time in an isotropic Potts grain growth model (+). The solid line approximates the steady state value (1.6245±0.0041).

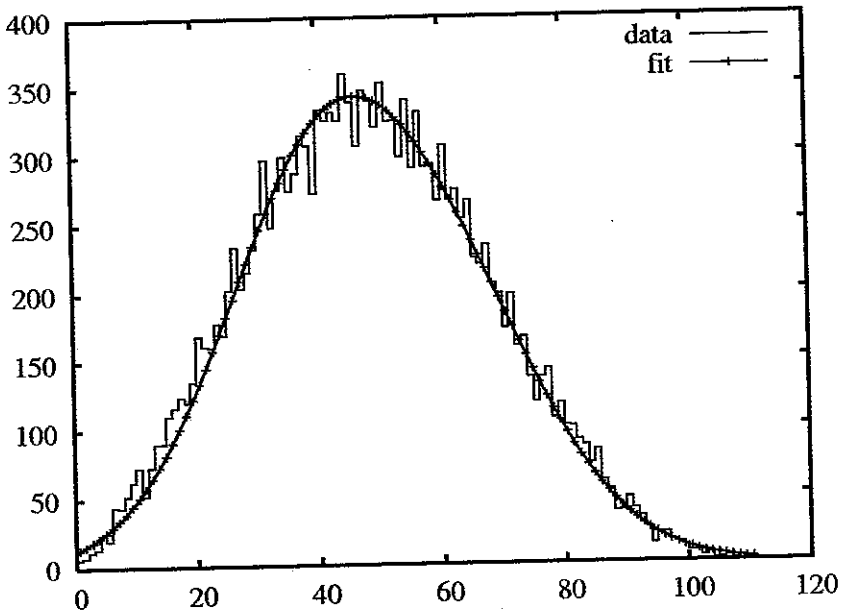

Fig. 8. Histograms of the distribution of mean width values for grains in an isotropic Potts grain growth model.

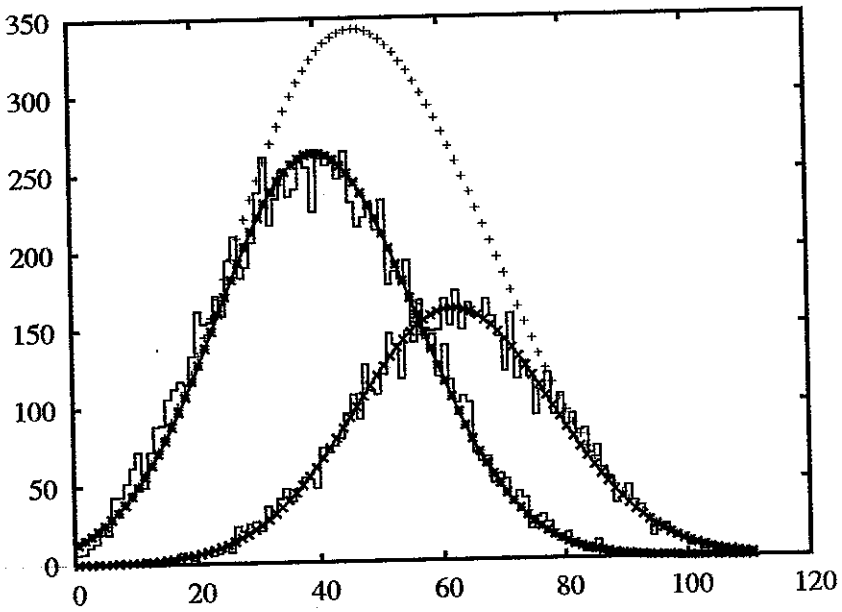

Fig. 9. Histograms of the distribution of mean width values for both growing grains and shrinking grains in an isotropic Potts grain growth model. The two subsets of grains have mean width distributions close to bell-curves, also shown. The mean width distribution for the total population is outlined in the background.

Summary: Mean width algorithm: O&M's algorithm performs very well for all morphologies and orientations, given sufficient resolution. When much of the surface curvature is contained along a crease, the algorithm is limited by the ability to sufficiently resolve the dihedral angle defining the crease. Further increasing the accuracy of the spherical integration does not lead to great improvement, and can actually degrade the performance of the algorithm. Poor performance at low resolution is to be expected, but given the non-negligible population of very small grains in many realistic microstructures, it is important to address the issue of improving accuracy in this limit. The modified algorithm, noted as MW211, offers improved speed and accuracy for most shapes.

2. ANALYZING BOUNDARY MOTION IN 3D

In papers by Lienert *et al.* (2010), in this same Symposium, and Hefferan *et al.* (2010, *ibid.)* and Suter *et al.* (2006), a High Energy Diffraction Microscopy (HEDM) method is described of using synchrotron radiation to probe microstructures non-destructively in 3D. Given that all the pertinent details of the technique are described in this same volume, we will describe preliminary results of an experiment to measure grain boundary motion in 3D and the analysis of the character of the grain boundaries involved. In brief, a high energy x-ray beam illuminates a layer of a cylindrical sample, which latter is rotated in front of the beam so that diffractograms at three different offsets from the sample can be measured on 0.5° intervals. The resulting dataset is analyzed using a forward modeling method to assign an orientation to each point on a regular grid in the illuminated layer. This process is repeated for each layer for as many layers as required in order to build up a 3D image. Each point is indexed independently and so when compact regions are observed with similar orientations in an annealed polycrystal, it is clear that the grain structure is being correctly characterized.

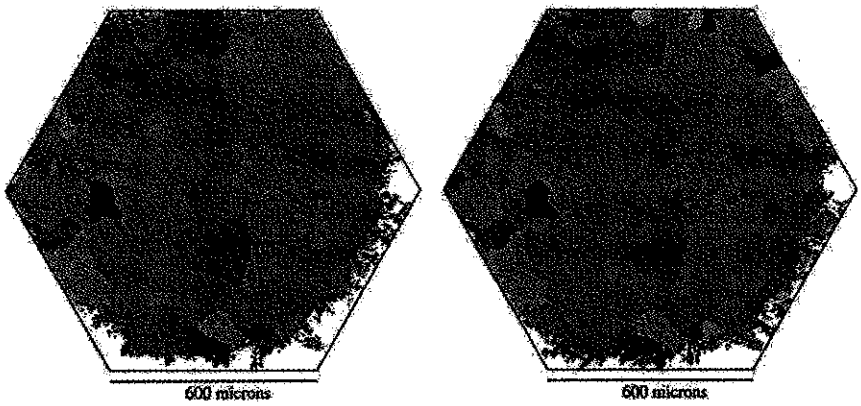

(a) (b)

Fig. 10. (a) Microstructure of Al wire before annealing and (b) microstructure after annealing. Each point is colored according to the components of the Rodrigues vector that describes the orientation.

A grain growth experiment was performed by first characterizing a polycrystalline aluminum wire sample using HEDM. Eleven layers were measured and analyzed; the resolution is given below. The grain size was of the order of 150 microns, in a cross section of order 600 microns diameter. Each layer spans the entire cross-section of the wire. The sample was then exposed to

elevated temperature in order to induce grain growth by annealing in increments of about 8°C for ten minutes, then allowing the microstructure stabilize to room temperature. The final anneal put the sample at ~70°C for about 15-20 minutes,. A representative layer is shown both before and after the annealing in Fig. 10, which at first glance suggests that there was no change in the grain boundary network.

That there was, in fact, boundary motion is most easily seen in Figure 11, which shows the difference in orientation (reduced to a rotation or misorientation angle), point by point, in the same slice through the structure. Most points did not change orientation. Those points that did change orientation are located next to a grain boundary, so grain boundary motion is clearly detectable from the orientation change in their wake. Only about 20% of the boundaries in the measured volume exhibited appreciable motion.

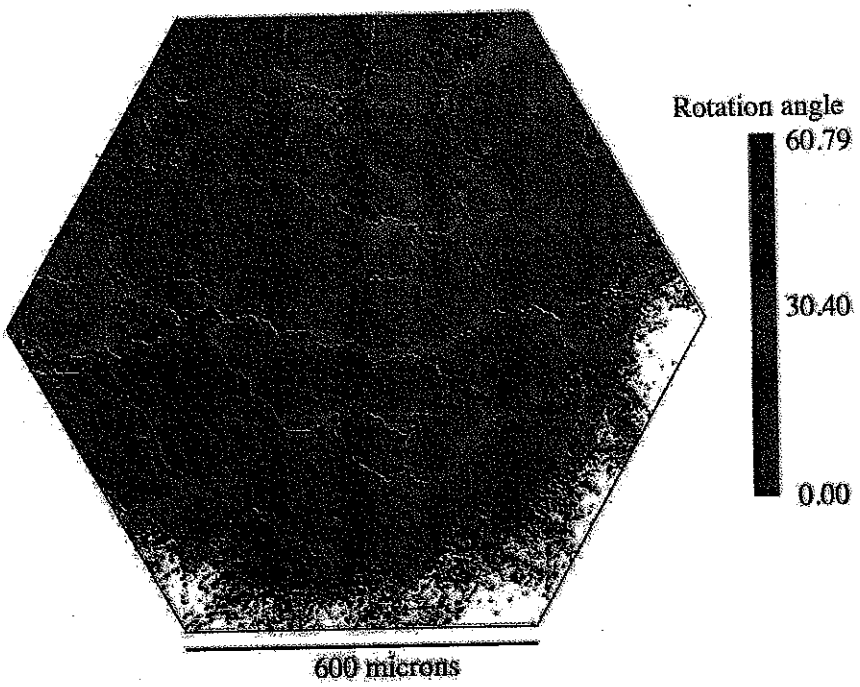

Fig. 11. Differential plot of the microstructure of the Al wire in layer 10, before and after annealing. Each point is colored according to the extent of orientation change during the annealing experiment. Boundaries that have moved are evident from the orientation change in their wake.

In order to analyze the grain boundary character, the image was analyzed with the help of the CGAL package (2010). This computational geometry package has a variety of tools for analysis of images and generation of meshes. Boundary points were interpolated between layers due to the anisotropic nature of the resolution, with 20 microns between layers versus 4 microns in-plane resolution. The resulting points were then smoothed using a 10 micron radius averaging filter, i.e., boundaries were re-sampled so that each sampled point is located at the average position of the nearest neighbors within a 10 micron radius. The Point Set Processing tools were used to extract grain boundary normals directly from the image and sorted according to the extent of boundary motion, Pierre *et al.* (2010). All boundary points moving more than 10 microns across annealed states are considered to have non-zero boundary motion. The 3D mesh

is generated by first converting our triangular grid of approximately 4 micron resolution into a rectangular grid of 2 microns. The 3D Mesh Generation tool was used on the voxelized data set to generate a surface mesh that represents the grain boundary network, Rineau *et al.* (2010). No further clean up or smoothing was done to the boundaries of the 3D mesh. The normal for each boundary was then transformed from the measurement frame to the local crystal frame for each side. Figure 12 shows the distribution of normals for (a) the set of boundaries that did not move and (b) the set of boundaries that did exhibit measurable motion. For this plot, lattice misorientation is not considered and, given the cubic crystal symmetry of aluminum, only one stereographic triangle is required to represent the normals. The two distributions are similar but (close-packed) {111} planes are more represented in the sessile boundaries whereas {100} planes are favored by the mobile boundaries.

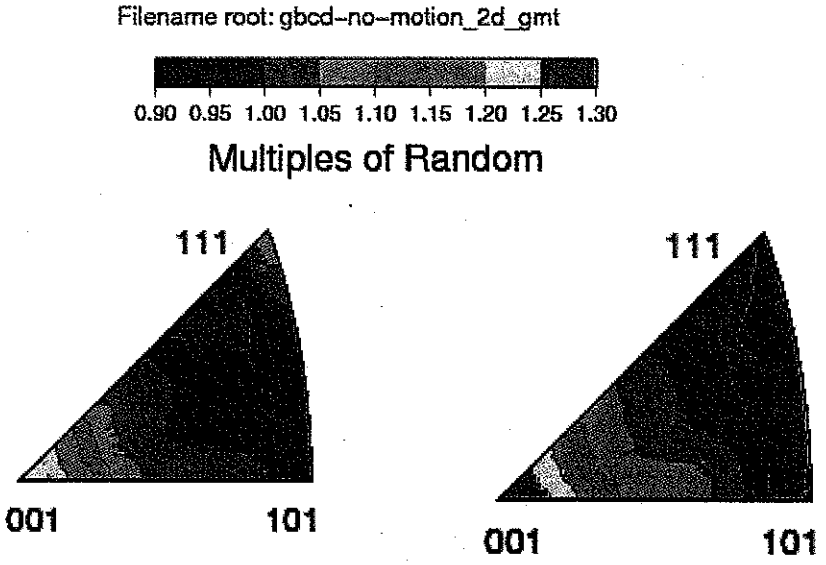

Fig. 12(a). Grain boundary normals for those boundaries that did not exhibit any measurable motion during grain growth.

Fig. 12(b). Grain boundary normals for those boundaries that moved during grain growth.

We can also analyze grain boundary behavior in greater detail, according to the full five degrees of freedom of grain boundaries. This topic been thoroughly explored in a number of different materials by first defining a suitable combination of the parameters. We follow the previously established convention of first binning by lattice misorientation and plotting a stereogram for each misorientation that displays the population of boundaries or some property. Misorientations were binned in Euler space, using the cosine of the second angle to obtain constant volume cells and normals were binned in spherical angles, again using the cosine of the co-latitude angle for constant cell area. A resolution of 10° in all five parameters was used and the units are multiples of a random (uniform) density. Figure 13 shows two such sets of boundary populations for the Σ3, Σ5, Σ7, Σ9, Σ11, Σ13b, Σ19a, Σ27a, and Σ27b types, again divided into those that did not move, Fig. 13a and those that did exhibit motion, Fig. 13b. The [100] direction points to the right (east) in each figure, [010] up (north) and [001] out of the page. The misorientation axis is located near to [100], in the [100]-[110]-[111] triangle, such that pure twist boundaries have normals coincident with the misorientation axis and pure tilt

boundaries are perpendicular to the axis. The Σ3 type is present above random in the sessile boundaries but less so for the boundaries that moved; the pattern in each stereogram is similar. For Σ5 boundaries, the two distributions are almost complementary with more tilt boundaries moving, and more twist boundaries sessile. Σ7 boundaries are more frequent in moving boundaries and are close to tilt configurations. In the Σ9, Σ11, Σ19a and Σ27a types, there are more moving boundaries with {100} normals (hence, mixed tilt-twist) compared to the sessile boundaries; the Σ19a type shows additional normals in the moving boundaries approximately on a small circle between (100) and (010). The distributions of the Σ13 boundaries is close to random in both cases although there is hint of a similar pattern to that observed for the Σ7 type. The distributions for the Σ27b type are non-random and similar for the moving and sessile boundaries.

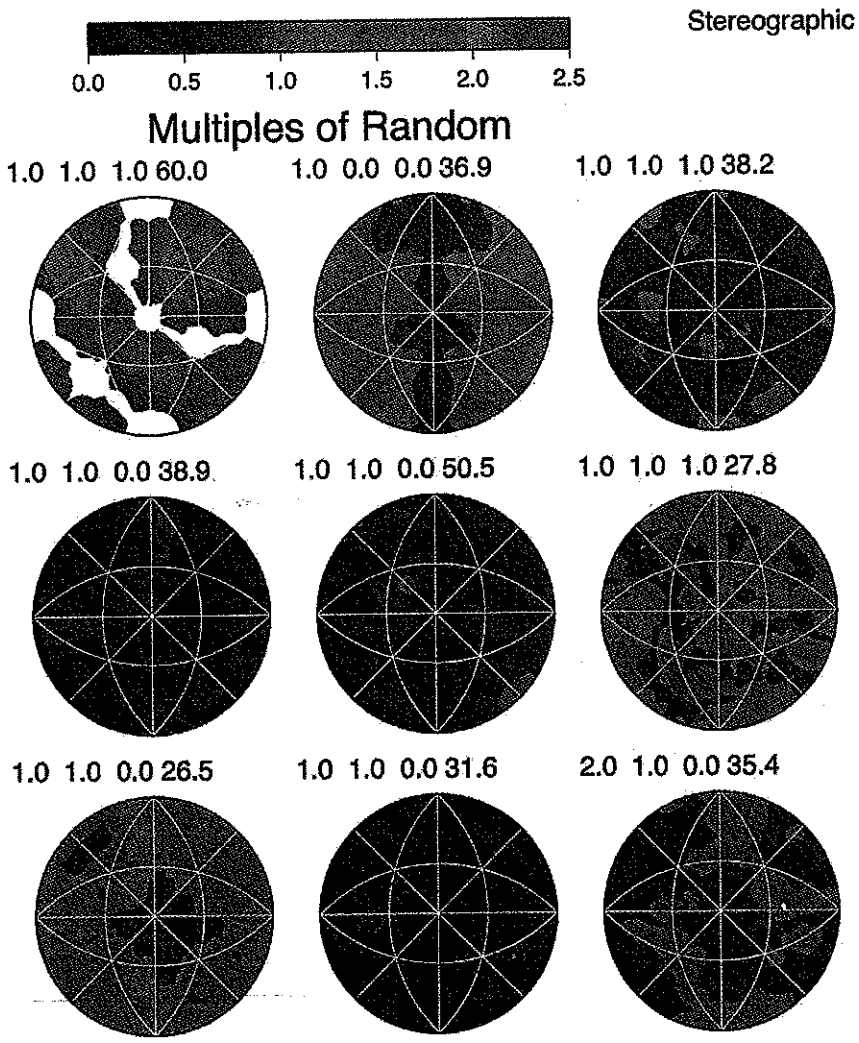

Fig. 13. (a) Grain Boundary Character Distribution of the boundaries that did not move, for several different CSL boundary types. From top left to bottom right, the misorientation types are Σ3, Σ5, Σ7, Σ9, Σ11, Σ13b, Σ19a, Σ27a, and Σ27b.

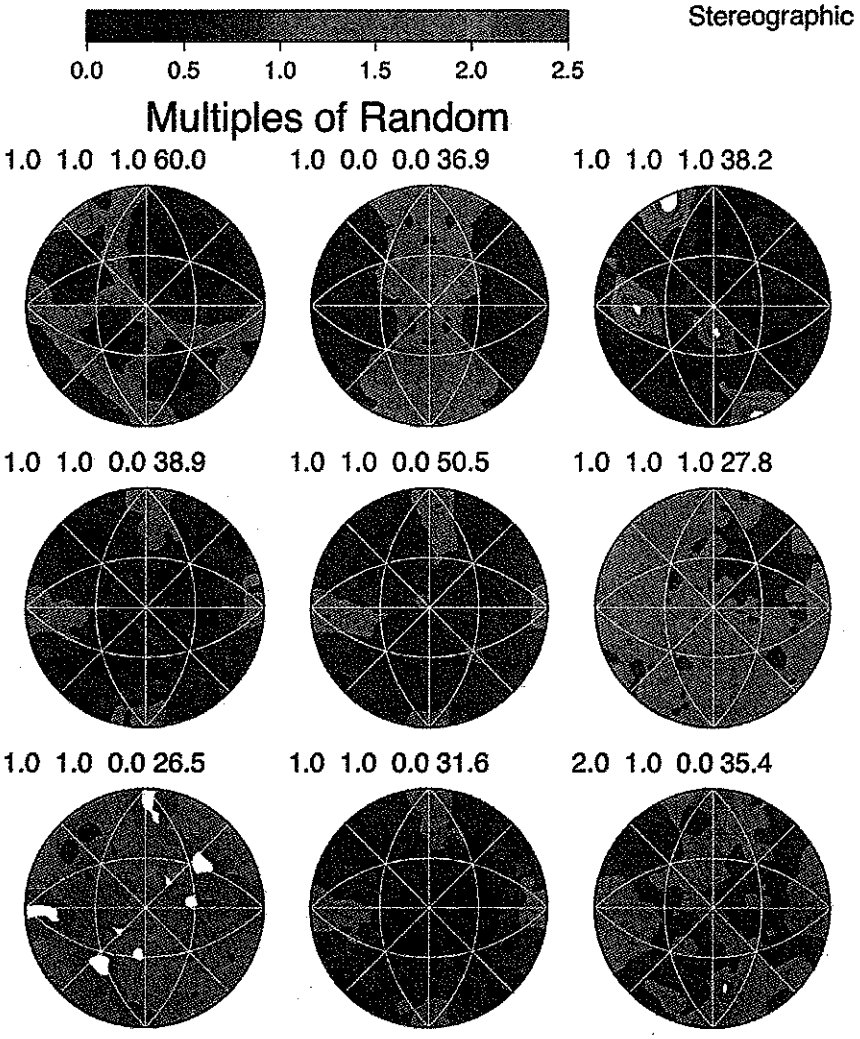

Fig. 13. (b) Grain Boundary Character Distribution of the boundaries that did move, for several different CSL boundary types. From top left to bottom right, the misorientation types are Σ3, Σ5, Σ7, Σ9, Σ11, Σ13b, Σ19a, Σ27a, and Σ27b.

3. SUMMARY

This paper has reviewed some examples of recent developments in characterization and analysis of microstructures and microstructural evolution in three dimensions. For analyzing the linear sizes of objects in images such as grains, the measurement of mean width has been described. For detailed examination of grain boundaries moving under the action of various driving forces, the application of five parameter grain boundary character distributions has been illustrated. Future work will aim to test the applicability of mean width measurement via use of the MacPherson-Srolovitz theory to quantitative modelling of grain growth. The analysis of grain boundary motion observed in experiments will be compared to both experimental and

theoretical literature. Olmsted et al. (2009) have, for example, published detailed results on grain boundary mobility in fcc metals using molecular dynamics. Especially at low temperatures, they found that some boundaries exhibited essentially negligible mobility. The observation that only certain boundaries moved may, however, have other physical origins such as the presence of low angle boundaries in certain grains that implies residual stored energy.

ACKNOWLEDGEMENTS

The support of the Office of Naval Research under grant number N000140610183, program manager J. Christodoulou, is gratefully acknowledged. Discussions with colleagues under the auspices of the Computational Materials Science Network (CMSN) under DOE/OBES support have been invaluable to this effort. Partial support of the MRSEC at CMU under NSF grant number DMR-0520425 is acknowledged.

REFERENCES

Alliez, P., L. Saboret, and N. Salman (2010). Point Set Processing, in CGAL User and Reference Manual. CGAL Editorial Board, edition 3.6.

CGAL - Computational Geometry Algorithms Library, http://www.cgal.org/, accessed April 2010.

Hadwiger, H. (1957). Vorlesungen über Inhalt, Oberfläche und Isoperimetrie, Springer Verlag.

Hefferan, C.M., Li, S.F., Lind, J., and Suter, R.M. (2010). Tests of Microstructure Reconstruction by Forward Modeling of HEDM Data. Advances in X-ray Analysis 53, Proc. of the 2009 Denver X-ray Conference, Powder Diffraction, *in press*.

Hefferan, C.M., Li, S.F., Lind, J., Lienert, U., Rollett, A.D., Wynblatt, P., and Suter, R.M. (2010). Statistics of High Purity Nickel Microstructure From High Energy X-ray Diffraction Microscopy. Computers, Materials and Continua, *in press*.

Klain, D.A. and Rota, G.-C. (1997). Introduction to Geometric Probability, Lezioni Lincee. Cambridge University Press.

Lienert, U., M.C. Brandes, J.V. Bernier, M.J. Mills, M.P. Miller, C.M. Hefferan, S.F. Li, J. Lind, R.M. Suter (2010). 3DXRD At The Advanced Photon Source: Orientation Mapping And Deformation Studies, Proc. 31st Intl. Risø Symposium, *in press*.

MacPherson, R.D. and Srolovitz, D.J. (2007). The von Neumann relation generalized to coarsening of three-dimensional microstructures. Nature, **446**, 1053–1055.

MMSP – Mesoscale Microstructure Simulation Project, http://matforge.org/cmu/wiki/mmsp, accessed May 2010.

Ohser, J. and Mücklich, F. (2000). Statistical Analysis of Microstructures in Materials Science, Wiley & Sons, pp. 107–124.

Olmsted D.L., Holm E.A., Foiles S.M (2009). Survey of computed grain boundary properties in face-centered cubic metals-II: Grain boundary mobility, Acta mater., **57**, 3704.

Rineau, L., S. Tayeb, and M. Yvinec (2010). 3D Mesh Generation, in CGAL User and Reference Manual. CGAL Editorial Board, edition 3.6.

Rollett, A.D., S.-B. Lee, R. Campman, G.S. Rohrer (2007). Three-Dimensional Characterization of Microstructure by Electron Back-Scatter Diffraction, Ann. Rev. Materials Research, **37**, 627-658.

Suter, R.M., Hennessy, D., Xiao, C., and Lienert, U. (2006). Forward Modeling Method for Microstructure Reconstruction Using X-ray Diffraction Microscopy: Single Crystal Verification. Rev. Sci. Instr. 77, 1-12.

Uchic M.D., Groeber M.A., Dimiduk D.M., Simmons J.P. (2006). 3D microstructural characterization of nickel superalloys via serial-sectioning using a dual beam FIB-SEM. Scripta mater. **55**, 23.

Uyar, F., S.R. Wilson, J. Gruber, S.-B. Lee, S.D. Sintay, A.D. Rollett and D.J. Srolovitz (2009). Testing a curvature driven moving finite element grain growth model with the generalized three dimensional von Neumann relation, International J. Materials Research, **2009**, 543-549.